



Overcoming concentration-dependence in responsive contrast agents for magnetic resonance imaging

Journal:	<i>Metallomics</i>
Manuscript ID:	MT-CRV-11-2014-000289.R1
Article Type:	Critical Review
Date Submitted by the Author:	19-Dec-2014
Complete List of Authors:	Ekanger, Levi; Wayne State University, Chemistry Allen, Matthew; Wayne State University, Chemistry

CRITICAL REVIEW

Overcoming the concentration-dependence of responsive probes for magnetic resonance imaging

Cite this: DOI: 10.1039/x0xx00000x

Levi A. Ekanger and Matthew J. Allen*

Received 00th January 2012,
Accepted 00th January 2012

DOI: 10.1039/x0xx00000x

www.rsc.org/metallomics

In magnetic resonance imaging, contrast agents are molecules that increase the contrast-to-noise ratio of non-invasively acquired images. The information gained from magnetic resonance imaging can be increased using responsive contrast agents that undergo chemical changes, and consequently changes to contrast enhancement, for example in response to specific biomarkers that are indicative of diseases. A major limitation with modern responsive contrast agents is concentration-dependence that requires the concentration of contrast agent to be known: an extremely challenging task *in vivo*. Here, we review advances in several strategies aimed at overcoming the concentration-dependent nature of responsive contrast agents.

Introduction

Magnetic resonance imaging (MRI) is a staple of modern diagnostic medicine and preclinical research because of its non-invasive nature and exquisite spatial resolution (0.025 mm isotropic resolution in preclinical scans).¹ The contrast-to-noise ratio of MRI scans can be enhanced with the use of exogenous molecules called contrast agents, often paramagnetic compounds, that interact with nearby nuclei (¹H is the most commonly detected), resulting in darker or brighter pixels in an image. The intensity of pixels in a conventional MRI image correlates to the amount of time—longitudinal (T_1), transverse (T_2), or both—needed for the nuclear dipoles of protons to realign with the external magnetic field (generated by the scanner) after the nuclear dipoles have been misaligned by a radiofrequency pulse (also generated by the scanner). Paramagnetic contrast agents, endowed with their own local magnetic field, can catalytically expedite the realignment, or relaxation, by interacting with numerous water protons through the exchange of water molecules or protons. Every contrast agent, even if structurally similar, produces contrast to different extents in MRI, and the behavior of paramagnetic contrast agents has been modeled and understood through the modified Solomon–Bloembergen–Morgan theory.² With the predictive power of this theory, chemists have performed a great deal of research with the goal of optimizing contrast agent efficiency [longitudinal (r_1) or transverse (r_2) relaxivity],^{3–10} which is a measure of the ability to relax protons as a function of the concentration of a contrast agent. Accordingly, the enhanced relaxation time brought about by a contrast agent is inherently dependent upon the concentration of a contrast agent. This dependence is one of the major limitations of contrast agents that change in response to specific stimuli.

Some of the earliest efforts toward developing responsive MRI contrast agents revolved around protein binding, which often caused relatively large increases in relaxivity.^{2b} The first reported enzyme-responsive contrast agent, the galactopyranose-functionalized gadolinium(III)-containing complex **1a** (Figure 1), was introduced by Meade and co-workers and responded to the presence of β -galactosidase to form **1b** with a 20% increase in r_1 .¹¹ In a separate report using **2a** (Figure 1), the same group observed a 77% change (3.26 to 5.76 mM⁻¹ s⁻¹) in r_1 in response to changes in the concentration of calcium ions resulting in the formation of **2b**.¹²

Since these seminal reports, many other responsive contrast agents for MRI have been developed that respond to a wide range of stimuli including changes in pH,^{13–33} temperature,^{32–37} metal ion concentration,^{12,38–40} and redox-active species.^{41–48} Many responsive contrast agents are designed with the goal of improving diagnostic capabilities *in vivo*. When performing *in vivo* imaging, however, the response of a contrast agent is meaningful only when the concentration of the contrast agent is known. To illustrate this point, the relaxivities of **2a** and **2b** have been plotted to exemplify the differences between *in vitro* (Figure 2) and *in vivo* (Figure 3) experiments. For *in vitro* experiments, the concentration of the contrast agent can easily be determined; therefore, the readout of $1/T_1$ can be used to determine if a contrast agent has responded. With *in vivo* studies, the concentration of contrast agents cannot be easily determined; therefore, when $1/T_1$ is measured during the imaging experiment, it is currently impossible to differentiate between a complete response, no response, or a partial response. This concentration-dependent nature holds true for many responsive contrast agents that have not been specifically designed to address the issue of concentration-dependence.

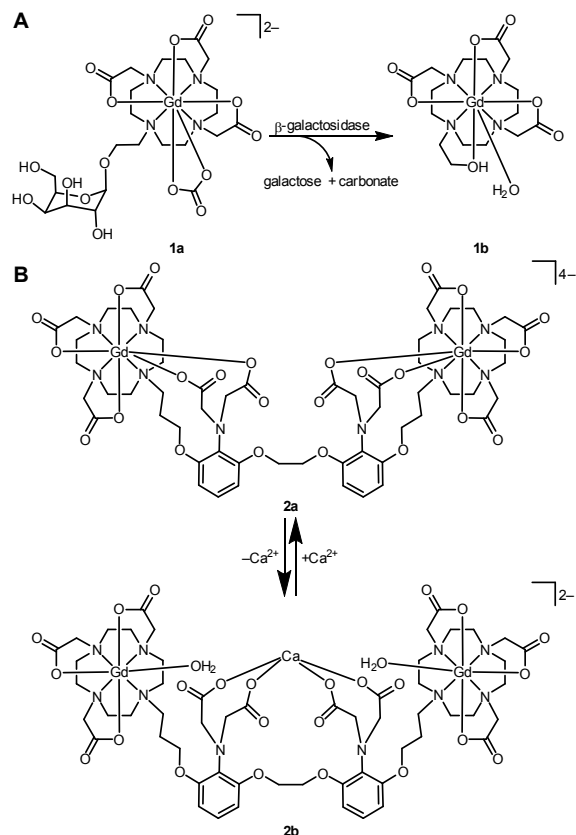


Figure 1. **A.** The first responsive contrast agent. In the presence of β -galactosidase, a galactose unit is removed from the contrast agent to facilitate the coordination of a water molecule and, consequently, a change in contrast enhancement;¹¹ **B.** A contrast agent (**2a** to **2b**) that responds to changes in the concentration of calcium ions.¹²

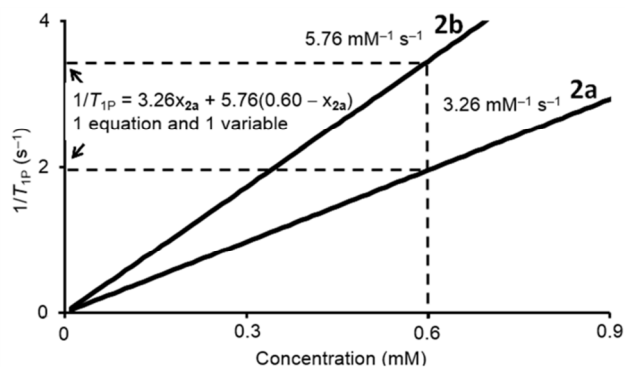


Figure 2. The relaxivities of **2a** and **2b** are the slopes of the lines of the paramagnetic contribution to relaxation rate ($1/T_{1P}$) as a function of the concentration of contrast agent. The plots illustrate the relaxivity in the presence (**2b**, $5.76 \text{ mM}^{-1} \text{ s}^{-1}$) and absence (**2a**, $3.26 \text{ mM}^{-1} \text{ s}^{-1}$) of calcium ions.¹² Relaxivity (slope of a linear function) can be expressed as an equation in the form of $1/T_{1P} = r_1x + b$ (in this example $b = 0$ because only the paramagnetic contribution is being plotted), where r_1 is the relaxivity or slope of the line and x is the concentration of the contrast agent. When calcium is present, the concentrations of **2a** and **2b** can be expressed as x_{2a} and x_{2b} , and the linear equation becomes $1/T_{1P} = (r_1^{2a})x_{2a} + (r_1^{2b})x_{2b}$. The vertical dashed line is a visual guide to demonstrate that a known

concentration of contrast agent (in this example 0.60 mM was arbitrarily selected) permits $1/T_{1P}$ measurements (horizontal dashed lines) to indicate the absence (2.0 s^{-1}) or presence (3.5 s^{-1}) of calcium. When the initial concentration of contrast agent bound to calcium is known (0.60 mM), the total concentration will remain 0.60 mM because the volume of a sample (*in vitro*) is constant. Accordingly, the total concentration of contrast agent bound to calcium can be expressed as $x_{2b} = 0.60 \text{ mM} - x_{2a}$. Substituting for x_{2b} in $1/T_{1P} = (r_1^{2a})x_{2a} + (r_1^{2b})x_{2b}$ yields $1/T_{1P} = (r_1^{2a})x_{2a} + (r_1^{2b})(0.60 \text{ mM} - x_{2a})$, which is solvable because there is one equation and one variable. In this example, the $1/T_{1P}$ values for **2a** and **2b** are boundaries, and the actual value can fall anywhere between the two boundaries. However, the $1/T_{1P}$ equation is solvable even for incomplete conversions between **2a** and **2b**.

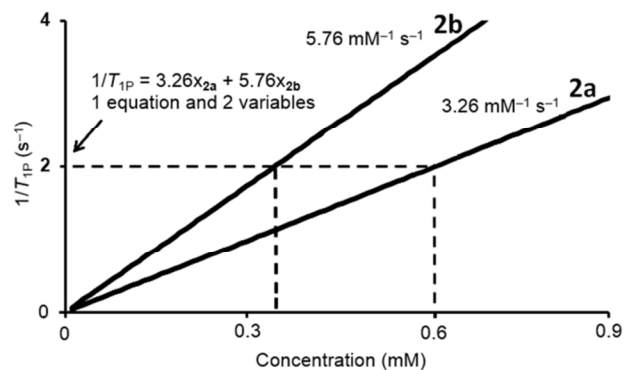


Figure 3. The relaxivities of **2a** and **2b** plotted as in Figure 2, where $1/T_{1P} = (r_1^{2a})x_{2a} + (r_1^{2b})x_{2b}$. The horizontal dashed line is a visual guide to demonstrate that a measured $1/T_{1P}$ value (in this example 2.0 s^{-1} was arbitrarily selected) can be produced by a 0.6 mM solution of **2a**, a lower concentration of **2b**, or a mixture of **2a** and **2b**. Without knowing the concentration of at least one of the contrast agents or the total amount of the two agents, the equation for $1/T_{1P}$ contains two unknown variables (x_{2a} and x_{2b}) and, consequently, cannot be solved.

In this review, we describe strategies used to design responsive contrast agents that are concentration-independent. Responsive contrast agents have been reviewed elsewhere,^{49–68} but this review is unique because our focus is on overcoming concentration-dependence in responsive contrast agents for MRI. Specifically, we focus on strategies that complement the depth penetration of MRI, including ratiometric chemical exchange saturation transfer, ratiometric relaxation rates, dual-mode imaging, dual-injection, and ligand field induced chemical shift strategies from the year 2000 to present.

Strategies for Concentration-Independence

Ratiometric Chemical Exchange Saturation Transfer

In contrast-enhanced T_1 -weighted MRI, contrast agents influence the relaxation times of nearby protons. The process is catalytic because of the relatively fast rate of exchange between coordinated and bulk water protons, resulting in interactions with a large number of protons in a short period of time. If, however, a contrast agent alters the chemical shift of exchanging protons such that the shift is distinguishable from the proton resonance of bulk water, a different mechanism of contrast can be generated. By selectively saturating the chemically-shifted protons with a radiofrequency pulse, the

intensity of the signals from these protons are diminished. During the saturation event, the shifted protons continue to exchange with bulk water through water or proton exchange. The net result is a transfer of nuclear dipole saturation to the bulk water signal, which causes a reduction in intensity (Figure 4) that is used to generate an image.

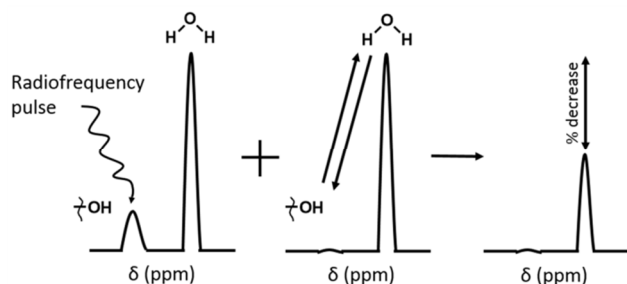


Figure 4. A simplified representation of chemical exchange saturation transfer (CEST) viewed as a ^1H -NMR spectrum. The signal from an exchangeable proton that is different from bulk water is reduced via a selective radiofrequency pulse while the proton is exchanging with protons in the bulk water. The combination of these two events results in a reduction of the signal intensity from bulk water, which can be measured and expressed as a percent decrease.

The reduction in bulk water signal intensity can be predicted by equation 1 (under the assumption that saturation time is long enough for an equilibrium to be established),⁶⁹ where M_S is the bulk water signal intensity after radiofrequency saturation at a given frequency, M_O is the bulk water signal intensity in the absence of a radiofrequency pulse, k_1 is the pseudo first-order proton exchange rate, and T_{1W} is the longitudinal relaxation time of bulk water. This contrast mechanism is called chemical exchange saturation transfer (CEST). One of the benefits of CEST is the ability to influence contrast upon demand, which is possible because CEST can only be measured after a selective, intentionally applied radiofrequency pulse. The ability to produce contrast upon demand is not possible with most other contrast agent modalities. Even with this benefit, the CEST effect is still dependent upon contrast agent concentration as seen in equation 2,^{69a} where n is the number of exchange sites on the contrast agent, k_{CA} is the proton exchange rate constant, and $[\text{CA}]$ is the concentration of contrast agent. The issue of concentration was circumvented for pH detection by Balaban and co-workers by using either the ratio of two different proton-exchange sites on **3** or exchange sites on two molecules, **4** and **5**, in the same solution (Figure 5).^{69a} The key to this ratiometric method was that each proton-exchange site had a unique pH dependence, which was determined by $\text{p}K_a$ values. Two unique exchange sites with non-equivalent pH dependence produce two distinct CEST signals, and the decrease in bulk water signal intensity for each site can be predicted with equations 3 and 4,^{69a} where S1 and S2 denote the first and second exchange sites. A ratio of the two CEST effects (the quotient of equations 3 and 4) yields equation 5.

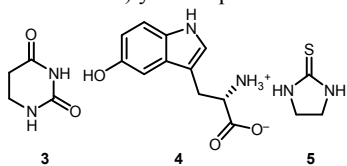


Figure 5. Structures of 5,6-dihydrouracil (**3**), 5-hydroxytryptophan (**4**), and 2-imidazolidinethione (**5**) used to demonstrate the first ratiometric CEST response to pH.^{69a}

$$M_S/M_O = (1 + k_1 T_{1W})^{-1} \quad (1)$$

$$k_1 = [\text{CA}]n k_{CA} \quad (2)$$

$$[(M_O - M_S)/M_S]^{S1} = [\text{CA}]^{S1} n^{S1} k_{CA}^{S1} T_{1W} \quad (3)$$

$$[(M_O - M_S)/M_S]^{S2} = [\text{CA}]^{S2} n^{S2} k_{CA}^{S2} T_{1W} \quad (4)$$

$$\frac{[(M_O - M_S)/M_S]^{S1}}{[(M_O - M_S)/M_S]^{S2}} = \frac{[\text{CA}]^{S1} n^{S1} k_{CA}^{S1}}{[\text{CA}]^{S2} n^{S2} k_{CA}^{S2}} \quad (5)$$

If the two exchange sites reside on separate molecules, knowledge of the concentration of the two molecules is still required because they cannot necessarily be assumed to be equal. However, if both exchange sites reside within the same molecule, the concentration cancels out on the right side of equation 5, thus circumventing the requirement of knowing concentration. With unique pH dependencies, calibrated ratios of CEST effects were used to determine the pH of a solution without knowledge of concentration. Soon after the initial report of the ratiometric CEST technique, other groups designed ratiometric CEST contrast agents that incorporated Ln^{3+} ions to induce large chemical shifts.^{21,22,34}

Ratiometric CEST with paramagnetic compounds. Often, the more a CEST signal is shifted downfield or upfield from bulk water, the more suitable it is for *in vivo* imaging. This idea is based on magnetization transfer effects that occur *in vivo* between bulk water and macromolecules (for example phospholipid membranes and proteins), which tend to broaden the *in vivo* bulk water signal.⁷⁰ Therefore, if CEST signals within this range are used, the contrast they provide can be drastically reduced or undetectable due to the magnetization transfer effects that occur during *in vivo* experiments. Recently, this notion has been challenged by reports of *in vivo* CEST imaging using saturation frequencies as close as 0.8 ppm from bulk water.⁷¹ Nevertheless, the development of many CEST agents has proceeded with the aim of pushing the chemical shift of exchangeable protons far from the bulk water proton signal. A separate reason for using CEST agents with relatively large chemical shifts is that the CEST effect is only observable when the chemical shift difference between chemically shifted and bulk water protons is greater than the proton-exchange rate. Accordingly, large chemical shifts tend to ensure that this requirement is met and allow contrast agents with relatively fast exchange rates to be used. To achieve large chemical shift offsets, lanthanide ions are routinely incorporated into contrast agents because of their ability to alter chemical shifts.⁷²

Interestingly, the ground state of Eu^{3+} (7F_0) does not have a magnetic moment and is diamagnetic despite having six unpaired f-electrons. However, some excited states are thermally accessible at room temperature (average magnetic moment ≈ 3.5 Bohr magnetons).⁷³ This thermally accessible paramagnetic behavior along with luminescent properties that allow for characterization of coordination environment, are at least two reasons why Eu^{3+} has been used in the design of CEST contrast agents.⁷⁴ Using a Eu^{3+} -containing contrast agent, Sherry and co-workers were able to observe the bound water protons on the DOTA-tetra(amide) derivative **6** (Figure 6) at ambient temperatures shifted 50 ppm downfield from bulk water.⁷⁵ Observing the bound-water proton resonance in an

aqueous solution was significant because previously Ln-bound water protons had only been observed on a Eu³⁺-containing complex in deuterated acetonitrile.⁷⁶ The ability to observe the bound-water resonance was recognized by Aime and co-workers as a step towards ratiometric CEST. Accordingly, Aime and co-workers hypothesized that the ability to detect both sets of protons (bound-water and amide) of Ln-tetra(amide) complexes would allow for a ratiometric CEST response that would be independent of the concentration of the contrast agent using the identical logic exploited by Balaban and co-workers in equation 5. Furthermore, Ln³⁺-containing complexes would increase the chemical shifts of both the bound water and amide protons to decrease or eliminate overlap with the broadened bulk water signal caused by magnetization transfer effects *in vivo*. Accordingly, Aime and co-workers investigated DOTA-tetra(amide) derivatives **7** through **12** to characterize the bulk water and amide proton resonances.²¹ Each complex displayed a unique amide proton chemical shift, but the complexes with the largest chemical shifts did not exhibit the most efficient saturation transfer because of differences in the longitudinal relaxation time of coordinated water protons.

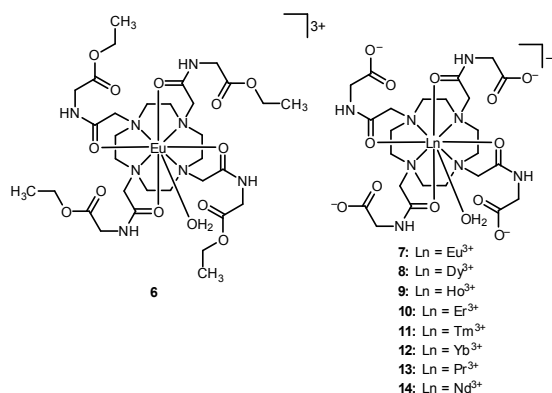


Figure 6. Structures of LnDOTA-tetra(amide) complexes.^{21,22,75}

Interestingly, in Aime's study, **12** had the highest saturation transfer at 70% despite only shifting the amide proton signal 16 ppm upfield from bulk water.²¹ Some lanthanides revealed an increase in saturation transfer (Figure 7) despite relatively small chemical shifts from bulk water. This phenomenon was attributed to different longitudinal proton relaxation times for each complex.²¹ With longer proton relaxation times, saturation transfer occurs to greater extents than with shorter times. Conversely, rapidly relaxing protons do not have enough time to transfer saturation to the bulk water proton pool. A striking example of this phenomenon was observed with **8**, where the complex shifted amide protons 77 ppm downfield from bulk water, but the relatively short longitudinal relaxation time of the metal complex caused the protons near Dy³⁺ to relax too quickly for saturation transfer to be observed (Figure 7).²¹ Taken together, it is a prime example that greater chemical shifts do not necessarily equate to greater CEST properties.

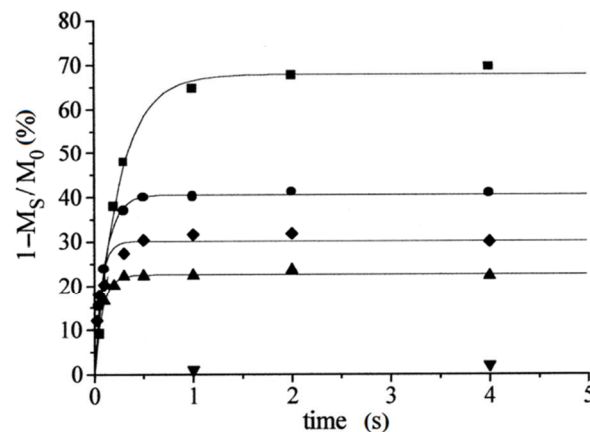


Figure 7. Percent saturation transfer as a function of radiofrequency irradiation time at the same saturation power ($B_1 = 25 \mu\text{T}$) for **8** (30 mM, ▼), **9** (30 mM, ▲), **10** (40 mM, ◆), **11** (40 mM, ●), and **12** (30 mM, ■) at 7 T, 312 K, and pH 8.1. Figure adapted with permission from Paramagnetic Lanthanide(III) Complexes as pH-Sensitive Chemical Exchange Saturation Transfer (CEST) Contrast Agents for MRI Applications/S. Aime, A. Barge, D. D. Castelli, F. Fedeli, A. Mortillaro, F. U. Nielsen and E. Terreno/*Magn. Reson. Med.*, 47/4. Copyright © 2002 Wiley-Liss, Inc.

$$\frac{[(M_0 - M_S)/M_0]^{YbL}}{[(M_0 - M_S)/M_0]^{EuL}} = \frac{4[YbL]k_{NH}^{YbL}}{2[EuL]k_{H_2O}^{EuL}} \quad (6)$$

Aime and co-workers followed their initial report with an investigation of **7**, **13**, and **14** to explore and, in the case of **7**, reinvestigate the relevant characteristics for single-molecule ratiometric CEST.^{22a} They found that each complex had observable amide and coordinated water protons that were capable of transferring saturation to bulk water, indicating that each complex could be used for single-molecule ratiometric CEST. The amide and coordinated water proton resonances at pH 7 from both studies are listed in Table 1, and the pH-dependence of saturation transfer can be seen in Figure 8. The saturation transfer of amide protons was affected by changes in solution pH; whereas, the saturation transfer of bound water protons was unaffected in the pH range of 5.5 to 7.5. Accordingly, **7**, **13**, and **14** were capable of reporting the pH of a solution without knowledge of contrast agent concentration using single-molecule ratiometric CEST. The sensitivity, however, was vastly different upon moving from low to high atomic numbers across the lanthanide series (Figure 8). Specifically, **13** had the largest and most sensitive ratiometric CEST ratio, and **7** had the least sensitive ratio. This phenomenon is reminiscent of the saturation transfer trend of **7** through **12**, where longitudinal proton relaxation time was attributed to the observed differences in saturation transfer regardless of the magnitude of the chemical shifts. Aime and co-workers performed additional characterization of the properties relevant to single-molecule ratiometric CEST using LnDOTAM-Gly complexes, which included a demonstration of a ratiometric temperature response that was independent of contrast agent concentration using **13** for *in vitro* studies.^{22b}

Table 1. Amide and bound water proton chemical shifts relative to bulk water of LnDOTAM-Gly complexes at pH 7. Both values are required for single-molecule ratiometric CEST.

Compound	Ln ³⁺	Amide ¹ H (ppm)	Bound H ₂ O ¹ H (ppm)	Ref.
13	Pr ³⁺	13	-70	22
14	Nd ³⁺	11	-50	22
7	Eu ³⁺	-4	40	21
8	Dy ³⁺	77	not observed	21
9	Ho ³⁺	39	not observed	21
10	Er ³⁺	-22	not observed	21
11	Tm ³⁺	-51	not observed	21
12	Yb ³⁺	-16	not observed	21

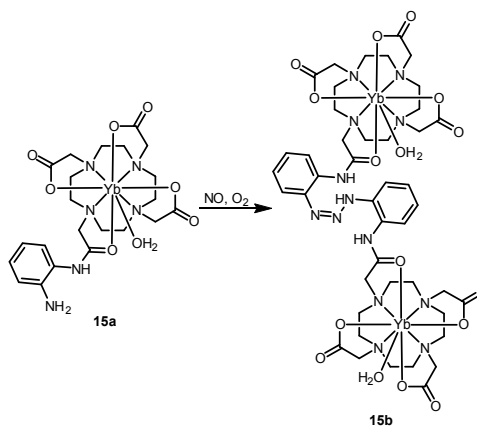


Figure 9. Structure of YbDO3A-oAA (**15a**) for pH and nitric oxide detection. The Yb³⁺-containing product of the nitric oxide and oxygen reaction is **15b**.^{23,47}

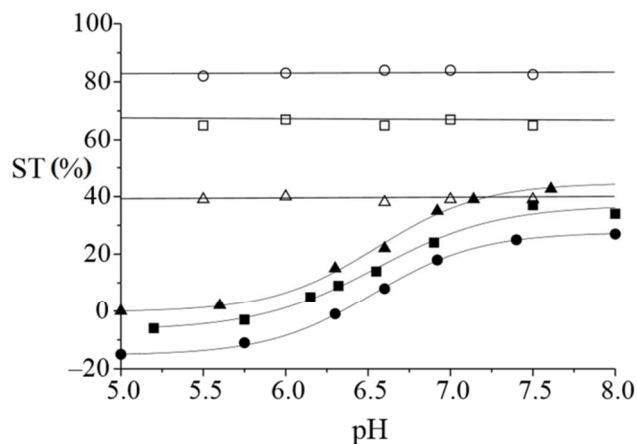


Figure 8. Saturation transfer (ST) as a function of pH for protons of amides (filled symbols) and coordinated water molecules (open symbols) for **7** (circles), **13** (triangles), and **14** (squares) at 7 T and 312 K after a 4 s irradiation. Figure adapted with permission from Novel pH-Reporter MRI Contrast Agents, S. Aime, D. D. Castelli and E. Terreno/*Angew. Chem.*, **114**/22. Copyright © 2002 WILEY-VCH Verlag GmbH & Co. KGaA, Weinheim.

In vivo ratiometric CEST imaging of pH was reported by Pagel and co-workers using **15a** (Figure 9).²³ After characterizing a concentration-independent pH response of **15a** using ratiometric CEST of the amide and amine protons, they injected **15a** directly into a tumor within a mouse. Using a minimum CEST threshold of 2% (corresponding to a 95% probability of the CEST effect being attributable to **15a**), an *in vivo* pH map was generated using the ratio of CEST effects after presaturation at 8 ppm downfield and 11 ppm upfield of bulk water.²³ The frequency offset of these CEST signals was serendipitous because magnetization transfer effects were thought to affect both signals equally because they are nearly symmetric about the bulk water signal. However, *in vivo* ratiometric imaging might be complicated using a signal shifted relatively close to water and a second signal shifted relatively far from bulk water. This complication might arise if magnetization transfer effects influence one of the signals to a greater extent than the other.

As evidenced through every example highlighted so far, pH is an intuitive target for responsive contrast agents because protons can be directly imaged with relatively high spatial resolution with MRI, and contrast agents can be readily designed with proton-exchange sites. Measuring pH with contrast agents relies on proton exchange because protons associated with the contrast agent must exchange with bulk water protons to generate contrast. Proton exchange is temperature-dependent and, consequently, pH measurements are inherently temperature-dependent. Sherry and co-workers developed single-molecule CEST temperature response without the use of ratiometric measurements.³⁴ Instead, they recognized that proton exchange is highly temperature-dependent and that small changes in the exchangeable proton chemical shift (hyperfine shifts) had the potential to report temperature using MRI. By measuring the bound-water proton exchange for **16** (Figure 10), they observed a drastic hyperfine shift from 800 to 650 ppm upfield from bulk water within a temperature range of 20 to 50 °C, while **7** exhibited smaller hyperfine shifts ranging from 55 to 45 ppm downfield of bulk water within the same temperature range. Sherry and co-workers chose **7** to demonstrate the temperature response in MRI (Figure 11), where the temporal resolution was about 3 min per experiment for each temperature.

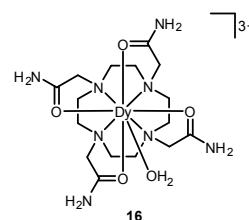


Figure 10. Structure of DyDOTAM (**16**) investigated for concentration-independent temperature response.³⁴



Figure 11. *In vitro* temperature maps (1 cm tube diameter) of a solution containing **7** (10 mM) at pH 7.0 with a calibrated color bar on the far right. T_{air} is the temperature of air flowing over the sample. Reprinted with permission from S. Zhang, C. R.

Malloy and A. D. Sherry, *J. Am. Chem. Soc.*, 2005, **127**, 17572. Copyright 2005 American Chemical Society.

Aime and co-workers combined pH and temperature response in dual-response contrast agent **17** (Figure 12), which, like other cyclen-based macrocyclic complexes that contain chiral centers, exists as a distribution of stereoisomers in solution.³³ Only two of the eight isomeric forms (see Figure 13 for all isomers) were observable through ¹H-NMR spectroscopy, and they were assigned as the *R* and *S* forms of one conformer. The hydroxyl protons of the two observable isomers of **17** occurred at 99 and 71 ppm downfield from bulk water. The ratio of the CEST effect for each isomer was used for ratiometric pH measurements (Figure 14) that were independent of the concentration of contrast agent. Additionally, the hyperfine shifts of each isomer responded linearly with temperature such that both shifts could individually report the solution temperature without knowledge of contrast agent concentration.

As previously mentioned, temperature affects ratiometric CEST measurements of pH because proton exchange is inherently temperature-dependent. The case is not so clear for using changes in hyperfine shift to measure temperature without a pH-dependence because protonation and deprotonation of functional groups on a complex can potentially alter chemical and conformational structure of the complex and lead to measurable changes in chemical shifts. It should be noted that a potential limitation with measuring hyperfine shifts for both of the previous examples is that multiple CEST images are required to scan a particular frequency range, which can increase total acquisition time. Longer MRI acquisition times are potentially limiting because the contrast agent is allowed more time to diffuse.

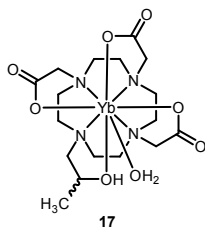


Figure 12. Structure of YbHPDO3A (**17**) used for concentration-independent detection of pH and temperature.³³

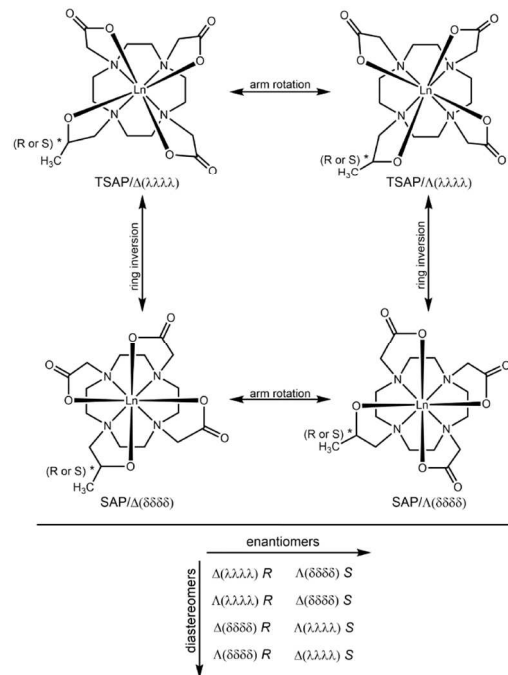


Figure 13. Twisted-square antiprism (TSAP) and square antiprism (SAP) isomeric forms of LnHPDO3A related to one another either through arm rotation or ring inversion. The bottom chart demonstrates eight possible isomers. Figure adapted with permission from Yb^{III}-HPDO3A: A Dual pH- and Temperature-Responsive CEST Agent/D. D. Castelli, E. Terreno and S. Aime/*Angew. Chem. Int. Ed.*, **50**/8. Copyright © 2011 WILEY-VCH Verlag GmbH & Co. KGaA, Weinheim.

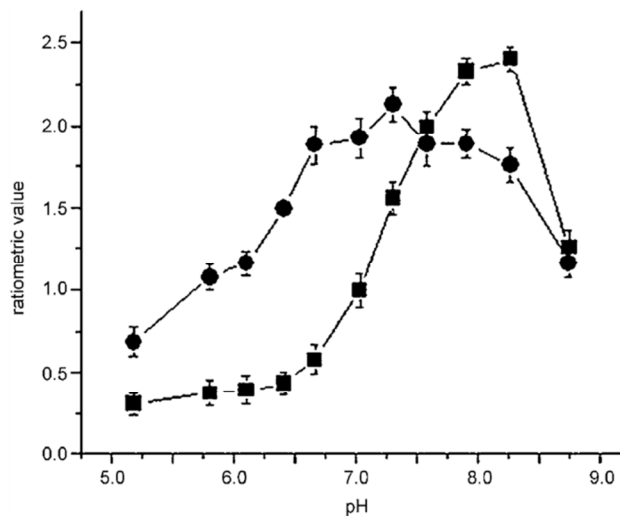


Figure 14. Ratiometric CEST values (calculated using the ratio of the CEST effect of each isomer) as a function of pH at 20 (■) and 37 °C (●). Error bars represent the standard deviation from the mean. Figure adapted with permission from Yb^{III}-HPDO3A: A Dual pH- and Temperature-Responsive CEST Agent/D. D. Castelli, E. Terreno and S. Aime/*Angew. Chem. Int. Ed.*, **50**/8. Copyright © 2011 WILEY-VCH Verlag GmbH & Co. KGaA, Weinheim.

1 Recently, Bartha and co-workers demonstrated a dual pH
 2 and temperature response *in vivo* that was independent of
 3 contrast agent concentration using **18** (Figure 15).³² They
 4 argued that using single-molecule ratiometric CEST is limited
 5 by the assumption that *in vivo* magnetization transfer effects
 6 will remain constant during the two separate CEST
 7 experiments. The assumption might be invalid when two
 8 different radiofrequency saturation powers are used. Using two
 9 saturation powers might cause magnetization transfer effects to
 10 be different from one anatomical region to the next, potentially
 11 altering the saturation transfer measurements. To circumvent
 12 this issue of heterogeneous magnetization transfer effects, they
 13 proposed using a magnetization transfer ratio asymmetry
 (MTR_{asym}) analysis to determine pH.

14 MTR_{asym} is a plot used to reveal asymmetric features in a
 15 CEST spectrum and is particularly useful for CEST signals that
 16 partially overlap with bulk water or endogenous tissue signal.
 17 The MTR_{asym} plot is generated by obtaining the difference in
 18 bulk water signal intensity at equal but opposite frequency
 19 offsets from bulk water. The net effect of this analysis is to
 20 remove the baseline saturation transfer to obtain a signal that
 21 corresponds to only one exchange site, allowing the linewidth
 22 of the CEST signal to be measured without interference from
 23 direct saturation of either bulk water protons or saturation
 24 transfer from endogenous tissues. Accordingly, Bartha and
 25 co-workers measured the MTR_{asym} linewidth of an amide CEST
 26 signal at 45 ppm upfield from bulk water using **18** and observed
 27 pH dependence from 6 to 8.³² Expectedly, the linewidth was
 28 also temperature-dependent because it is a function of exchange
 29 rate, but temperature was found to only influence linewidth
 30 between pH 7.5 and 8 at temperatures above 37 °C. A pH
 31 electrode was used to standardize the contrast agent response to
 32 pH prior to *in vivo* imaging. Many disease states coincide with
 33 pH values below 7, so the temperature dependence of linewidth
 34 was not considered a barrier to *in vivo* imaging. As seen in
 35 previous studies by other groups,^{33,34} the hyperfine shift varied
 36 with temperature to allow for accurate temperature
 37 measurements. Importantly, neither the MTR_{asym} linewidth nor
 38 the hyperfine shift of the signal were concentration-dependent.
 39 Using the aforementioned techniques, Bartha and co-workers
 40 successfully imaged *in vivo* pH and temperature using a single
 41 molecule (Figure 16) with average pH and temperature values
 42 of 7.2 ± 0.2 and 37.4 ± 0.5 °C.³² It should be noted that error
 43 within the *in vivo* CEST spectra were not reported. Similar to
 44 measuring hyperfine shifts, a limitation to the MTR_{asym}
 45 linewidth approach is that numerous frequency offset images
 46 are required to obtain enough data points to measure the
 47 linewidth, and acquiring more CEST images can substantially
 48 increase total acquisition time.

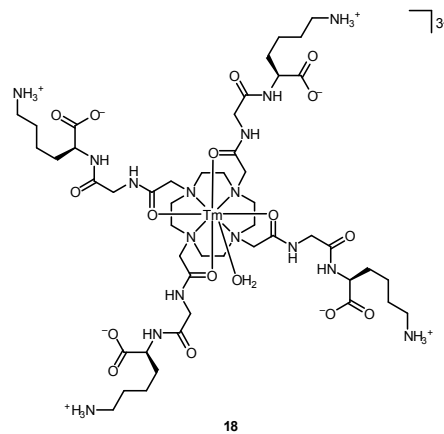


Figure 15. Structure of TmDOTAM-Gly-Lys (**18**) used for dual pH and temperature response that was independent of the concentration of contrast agent.³²

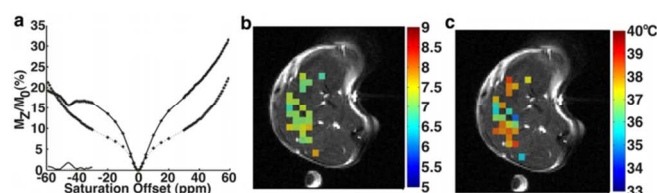


Figure 16. (a) CEST spectra of a mouse leg muscle generated pre- (solid line) and post-injection (dashed line) with MTR_{asym} (bottom left) post-injection at 45 ppm upfield from bulk water. Solid and dashed lines were generated using a tenth-order polynomial; (b) pH map superimposed onto a pre-injection image of the mouse leg muscle; and (c) temperature map superimposed onto a pre-injection image. Colored pixels represent regions exhibiting CEST contrast at ≥95% probability. Figure adapted with permission from Simultaneous In Vivo pH and Temperature Mapping Using a PARACEST-MRI Contrast Agent/N. McVicar, A. X. Li, M. Suchý, R. H. E. Hudson, R. S. Menon and R. Bartha/*Magn. Reson. Med.*, **70**/4. Copyright © 2012 Wiley Periodicals, Inc.

49 While lanthanides have been extensively used for
 50 concentration-independent measurements of pH, work by
 51 Morrow and co-workers has developed the use of d-block
 52 metals for the same purpose.²⁴ Using **19** (Figure 17) with Co²⁺,
 53 four unique amide resonances (112, 95, 54, and 45 ppm) were
 54 observed downfield of bulk water in the CEST spectrum. The
 55 four resonances were thought to be caused by two bound amide
 56 arms that are not related by symmetry. Interestingly, two of the
 57 amide resonances were found to have unique pH dependencies,
 58 which made them prime candidates for ratiometric pH
 59 response. Using the two most downfield signals at 112 and 95
 60 ppm, a linear relationship with pH was observed (Figure 18).
 The ratiometric pH response was not demonstrated to be
 independent of contrast agent concentration, but it was
 observed that the magnitude of CEST (not the ratio) was
 dependent on contrast agent concentration.

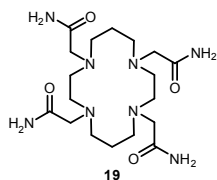


Figure 17. Structure of ligand **19** used for ratiometric pH detection with Co^{2+} .²⁴

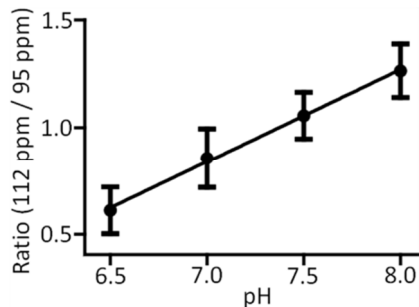


Figure 18. CEST ratio as a function of pH using the Co^{2+} -containing complex of **19** (4 mM) in 2-(*N*-morpholino)ethanesulfonic acid or 4-(2-hydroxyethyl)-1-piperazineethanesulfonic acid buffer (20 mM) with NaCl (100 mM). Measurements were recorded at 4.7 T and 37 °C. Error bars represent standard deviations of three measurements. Adapted from Ref. 24 with permission from The Royal Society of Chemistry.

As demonstrated through the highlighted examples in this section, significant progress has been made in concentration-independent imaging of pH and temperature. The choice of both pH and temperature responses can be explained by the ease of detecting protons in MRI and the inherent temperature-dependence of proton exchange. Although these two parameters were a good starting point, they are not the only important targets for concentration-independent response. For example, Pagel and co-workers made progress toward new targets for concentration-independent response by demonstrating nitric oxide response in the presence of oxygen using **15a**,⁴⁷ which underwent an irreversible reaction forming a triazene linkage between two equivalents of the contrast agent to form **15b** (Figure 9).⁴⁷ The measurements made by Pagel and co-workers using **15a** and **15b** were not deemed concentration independent, but the covalent incorporation of a secondary CEST agent that does not react with nitric oxide, such as **11**, could facilitate concentration-independent nitric oxide response.

Another example of a target other than pH or temperature was demonstrated by Sherry and co-workers who achieved a concentration-independent response to singlet oxygen using **20a** (Figure 19).⁴⁵ The incorporation of a 9-anthryl group facilitated an irreversible reaction with singlet oxygen to form **20b**, and the ~3 ppm (Figure 20) chemical shift difference between the amide protons before and after response enabled ratiometric CEST imaging. The use of CEST imaging allowed for the formation of singlet oxygen to be observed from the disproportionation of H_2O_2 catalyzed by MoO_4^{2-} (Figure 20b) because the CEST ratio is also a ratio of product over reactant. *In vitro* phantom images of singlet oxygen response enabled quantification of singlet oxygen after presaturation at 55 and 48 ppm downfield from bulk water.

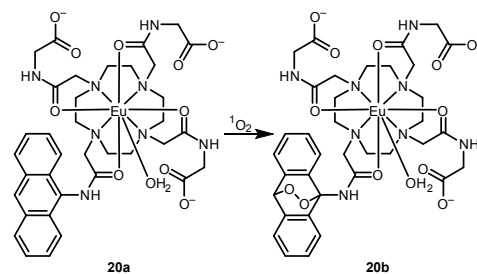


Figure 19. Structures of EuDOTAM-9A (**20a**) and the product of its reaction with singlet oxygen (**20b**).⁴⁵

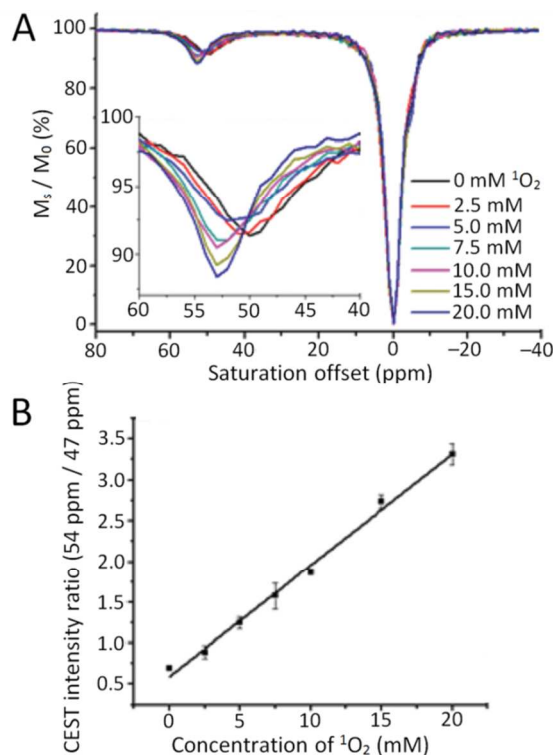


Figure 20. (A) M_s/M_0 as a function of saturation offset for increasing concentrations of singlet oxygen at 9.4 T and 298 K. Inset: Enlarged view. (B) CEST ratio as a function of concentration of singlet oxygen. Adapted from Ref. 45 with permission from The Royal Society of Chemistry.

A new ratiometric CEST method using different radiofrequency powers was recently reported by Aime and co-workers.⁷⁷ In this technique, a ratio, which has been named the ratio of radiofrequency power mismatch, is calculated by the quotient of saturation transfer at two different radiofrequency powers as seen in equation 7, where ST is the measured saturation transfer and $RF1$ and $RF2$ are the first and second radiofrequency powers used to measure saturation transfer. Importantly, radiofrequency power mismatch is dependent on pH (pH-dependence indicates temperature dependence as well, but this was not demonstrated in the report) and radiofrequency power, but it is independent of the concentration of contrast agent. Using the radiofrequency power mismatch approach, Aime and co-workers demonstrated both *in vitro* and *in vivo* pH detection using radiofrequency powers of 1.5, 3, and 6 μT .⁷⁷

$$\text{radiofrequency power mismatch} = \frac{[(1-ST)/ST]_{RF1}}{[(1-ST)/ST]_{RF2}} \quad (7)$$

The use of ratiometric imaging has worked well for contrast agents that produce two CEST signals with unique pH dependencies. The ratiometric approach, however, is not limited to CEST imaging applications. In the next section, we highlight examples of ratiometric imaging using relaxation rates.

Ratiometric Relaxation Rates

The absence of Gd^{3+} -containing contrast agents in the previous section is primarily due to the relatively slow electronic relaxation time (T_{1e}) of Gd^{3+} compared to other Ln^{3+} metal ions.² The result of a relatively slow T_{1e} is that Gd^{3+} will relax protons efficiently. In fact, Gd^{3+} relaxes nearby protons so quickly that complexes containing Gd^{3+} and exchangeable protons (amine, amide, hydroxyl, and bound water) will not exhibit CEST effect.⁷⁸ On the other hand, Gd^{3+} is an efficient positive contrast agent because it can drastically decrease the T_1 of nearby protons. However, as discussed in the introduction, merely changing the relaxivity of a Gd^{3+} -containing complex will impose a concentration-dependence on the response of the agent, which limits its practicality *in vivo*. Therefore, neither ratiometric CEST nor changes in relaxivity are sufficient for the design of concentration-independent responsive contrast agents containing Gd^{3+} . Instead, changes in both longitudinal and transverse relaxation rates can be used for ratiometric imaging.

Aime and co-workers proposed using the ratio between the transverse and longitudinal paramagnetic contribution to relaxation rates (R_{2p}/R_{1p}) as a concentration-independent handle for pH detection.²⁵ The transverse and longitudinal relaxation rates are the inverse of the transverse and longitudinal relaxation times T_2 and T_1 , respectively. The rationale for this approach can be explained using equations 8 through 10 (commonly used to describe bound water proton contributions to relaxation rates), where P_M is the mole fraction of water protons bound to Gd^{3+} ($[Gd]/55.6$), τ_M is the residence lifetime of the bound water protons, and T_{2M} and T_{1M} are the transverse and longitudinal relaxation times of the bound water protons. Individually, R_{1p} and R_{2p} are concentration-dependent because of P_M (equations 8 and 9), whereas P_M is cancelled in the ratio (equation 10). Neither T_{1M} nor T_{2M} are concentration-dependent, but they are both dependent on the rotational correlation time (τ_R).² Therefore, changes in τ_R are expected to cause changes in both T_{1M} and T_{2M} . Likewise, changes in T_{1M} and T_{2M} are expected to cause changes in the R_{2p}/R_{1p} ratio (equation 10), which remains concentration-independent. Accordingly, changes in τ_R are predicted to cause changes in the ratio of relaxation rates. The connection between τ_R and relaxation rates was used for pH response using **21** (Figure 21) by a reversible, conformational transition between α -helical and random coil conformers.²⁵ The change in conformation caused a change in τ_R , which caused a change in the ratio of relaxation rates. Using **21**, a ratiometric response to pH was demonstrated that was independent of the concentration of contrast agent (Figure 22).

$$R_{1p} \approx \frac{P_M}{T_{1M} + \tau_M} \quad (8)$$

$$R_{2p} \approx \frac{P_M}{T_{2M} + \tau_M} \quad (9)$$

$$\frac{R_{2p}}{R_{1p}} \approx \frac{T_{1M} + \tau_M}{T_{2M} + \tau_M} \quad (10)$$

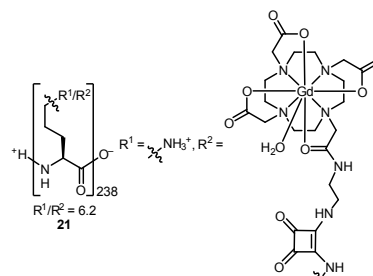


Figure 21. Structure of $[(GdDOTAam)_{33}-Orn_{205}]$ (**21**) used for concentration-independent pH measurements using ratiometric relaxation rates.²⁵

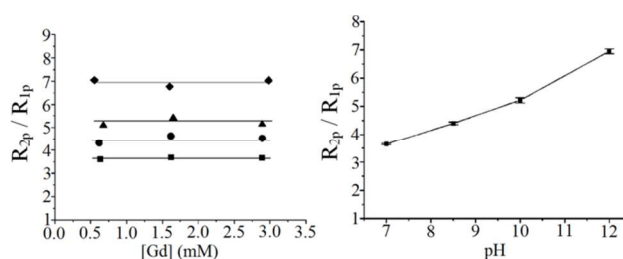


Figure 22. Left: Relaxation rate ratio as a function of Gd^{3+} concentration at pH 7 (■), 8.5 (●), 10 (▲), and 12 (◆). Right: Relaxation rate ratio as a function of pH. All measurements were recorded at 14 T and 25 °C. Adapted with permission from S. Aime, F. Fedeli, A. Sanino and E. Terreno, *J. Am. Chem. Soc.*, 2006, **128**, 11326. Copyright 2006 American Chemical Society.

In a recent study, Digilio, Aime, and co-workers applied the R_{2p}/R_{1p} approach to detect matrix metalloproteinase-2 activity.⁷⁹ Instead of relying on reversible changes to molecular conformation, an irreversible reaction was used to change R_{2p}/R_{1p} by an enzyme-catalyzed cleavage of a peptide. Before enzyme cleavage, **22a** (Figure 23) remained embedded within a liposome membrane, which forced the complex to have a relatively long τ_R because of the slow molecular reorientation of liposomes compared to small molecules.⁸⁰ Upon reacting with matrix metalloproteinase-2, **22b** was cleaved from the liposome membrane and, consequently, experienced a decrease in τ_R .⁷⁹ As discussed previously, changes in τ_R induce measurable changes in R_{2p}/R_{1p} that are independent of contrast agent concentration. By measuring R_{2p}/R_{1p} of **22a** embedded in liposomes exposed to matrix metalloproteinase-2, the activity was measured and the response was found to be independent of the concentration of contrast agent (Figure 24).

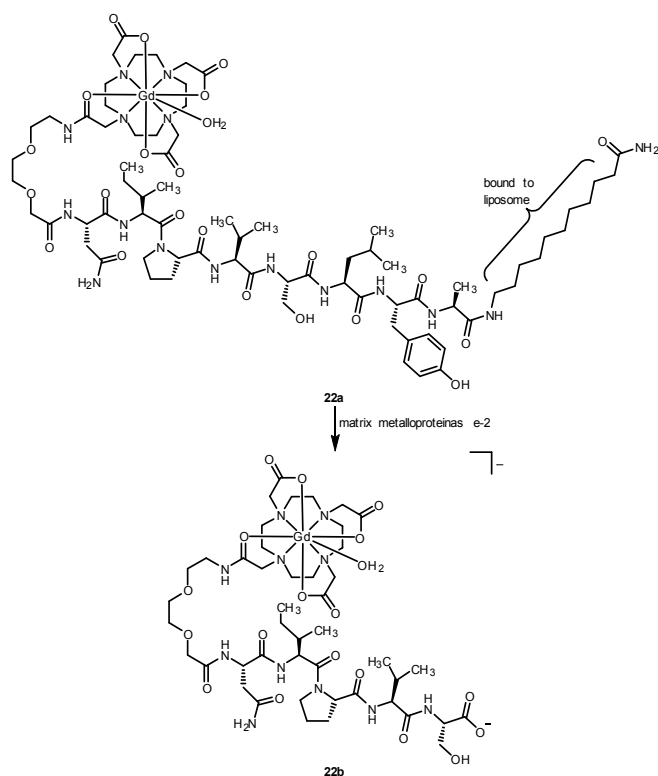


Figure 23. Structure of a contrast agent that is responsive to the activity of matrix metalloproteinase-2 before (**22a**) and after (**22b**) peptide cleavage by the enzyme.⁷⁹

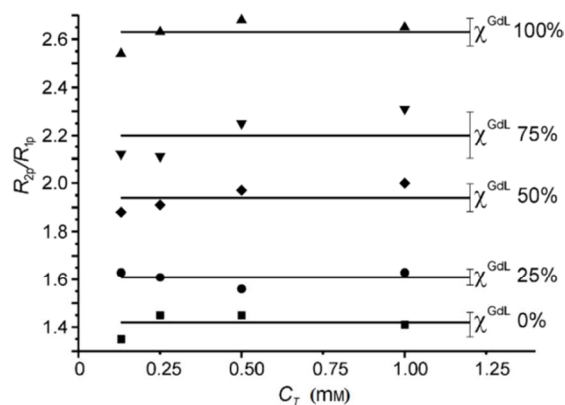


Figure 24. R_{2p}/R_{1p} as a function of contrast agent concentration (C_T) demonstrating concentration-independence and that R_{2p}/R_{1p} responds to decreasing mole fraction of **22a** (χ^{GdL}). Figure adapted with permission from A Ratiometric Procedure to Assess Matrix Metalloproteinase-2 Activity by Magnetic Resonance Imaging/V. Catanzaro, C. V. Gringeri, V. Menchise, S. Padovan, C. Boffa, W. Dastrù, L. Chaabane, G. Digilio and S. Aime/*Angew. Chem. Int. Ed.*, **52**/14. Copyright © 2013 WILEY-VCH Verlag GmbH & Co. KGaA, Weinheim.

In the previous examples of ratiometric relaxation rates, the authors observed that the R_{2p}/R_{1p} ratio was also dependent on external magnetic field strength. In a different report, a ratiometric approach to pH measurement was developed by

measuring R_{1p} at two different magnetic field strengths.²⁶ A magnetic field strength dependence can be seen in equations 11 and 12, where R_{1p} is determined through r_{1p} , which is field strength-dependent, and Gd^{3+} concentration at the respective magnetic field strengths (1 and 0.2 T). The ratio of R_{1p} at different magnetic field strengths (equation 13) cancels the requirement for Gd^{3+} concentration. Using the amphiphilic complex **23a** (Figure 25) in liposomes, Aime and co-workers were able to measure solution pH within 3.5% error compared to a pH electrode (Figure 26).²⁶ The mechanism of pH response was investigated using NMR dispersion profiles. It was proposed that acidic pH values facilitated the protonation of the sulfonamide nitrogen, which would prevent coordination to Gd^{3+} to leave vacant sites for water coordination. Furthermore, when the complex remains protonated and neutral, it can embed itself within the hydrophobic region of the liposome membrane causing an increase in membrane permeability. Upon changing the pH to alkaline values, the nitrogen of the sulfonamide arm could be deprotonated to form an anionic complex (**23b**). The anionic complex had less affinity for the hydrophobic region of the membrane and fewer vacant sites for water coordination. These reversible structural changes were used to explain differences in R_{1p} at different pH values. It should be noted that changing the external magnetic field strength has been previously used to highlight areas of an albumin-bound contrast agent *in vivo*.⁸¹

$$R_{1p}(1\text{ T}) = r_{1p}(1\text{ T}) \times [\text{Gd}] \quad (11)$$

$$R_{1p}(0.2\text{ T}) = r_{1p}(0.2\text{ T}) \times [\text{Gd}] \quad (12)$$

$$\frac{R_{1p}(1\text{ T})}{R_{1p}(0.2\text{ T})} = \frac{r_{1p}(1\text{ T})}{r_{1p}(0.2\text{ T})} \quad (13)$$

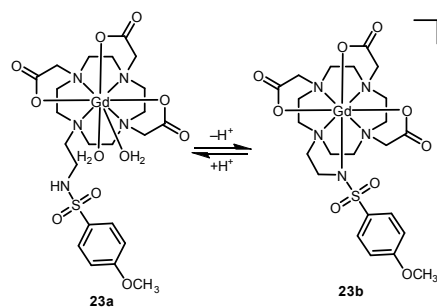


Figure 25. Structure of protonated (**23a**) and deprotonated (**23b**) GdDO3Asa used for ratiometric relaxation rate measurements at different magnetic field strengths for concentration-independent measurements of pH.^{26,28}

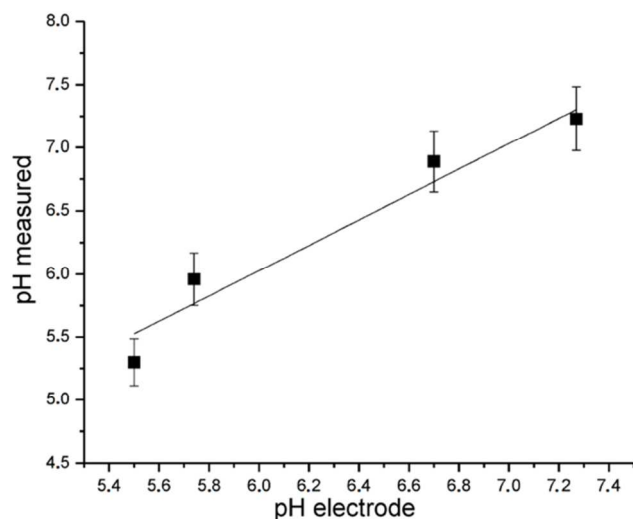


Figure 26. pH measured using liposome-encapsulated **22** and the ratiometric R_{1P} approach vs pH measured by an electrode. Adapted with permission from E. Gianolio, S. Porto, R. Napolitano, S. Baroni, G. B. Giovenzana and S. Aime, *Inorg. Chem.*, 2012, **51**, 7210. Copyright 2012 American Chemical Society.

In a cautionary tale, Pierre and co-workers attempted to use ratiometric relaxivity (r_1/r_2) of magnetic iron oxide nanoparticles to circumvent the need for contrast agent concentration.⁸² Briefly, magnetic iron oxide nanoparticles can be coated with organic substrates capable of inducing nanoparticle aggregation upon exposure to the desired target. The change in the relaxivity ratio before and after aggregation can be used to determine response, and the ratio of r_1/r_2 can be used to circumvent the need to know contrast agent concentration. While this technique had been previously reported using magnetic iron oxide nanoparticles for the detection of oligonucleotides,⁸³ antibodies,⁸³ enzymes,^{83,84} proteins,⁸⁵ and viruses,⁸⁶ Pierre and co-workers observed that aggregation does not result in a constant increase in transverse relaxivity, but rather produces a bell-shaped curve as a function of aggregate size. Therefore, they argued that using r_1/r_2 to measure the concentration of analyte without knowledge of contrast agent concentration is inaccurate for magnetic iron oxide nanoparticles.

While ratiometric techniques can be powerful when coupled with the appropriate contrast agent, there exists a separate option which does not require ratiometric measurements. To avoid ratiometric analysis, one can detect the contrast agent using different imaging modalities instead.

Dual-Mode

An alternative to using ratiometric methods for concentration-independent responsive contrast agents is to use two detection modes (dual-mode) for imaging. In dual-mode imaging, the contrast agent of interest can be detected using two or more imaging modes such as ^1H - (T_1 -weighted, T_2 -weighted, or CEST), ^{31}P -, and ^{19}F -MRI, positron emission tomography (PET), or single-photon emission computed tomography (SPECT). An attractive feature of dual-mode imaging is that one mode can be used to detect a response while the other mode can act to monitor the location of the contrast

agent and, in some cases, its concentration for quantification of the target molecule. Measuring the concentration of a contrast agent differentiates dual-mode imaging from ratiometric strategies to overcome concentration-dependence because determination of concentration is not possible or necessary using the ratiometric CEST or relaxation rate techniques described in the previous sections.

Aime and co-workers used a combination of ^{19}F - and ^1H -MRI for measuring pH by incorporating **24** and **25** (Figure 27) into poly- β -cyclodextrin (polymeric form of β -cyclodextrin consisting of 8–10 units).³⁰ It had been previously demonstrated that adamantane derivatives have a strong binding affinity for β -cyclodextrin,⁸⁷ and it was assumed that both **24** and **25** were anchored into the polymer through the adamantane moiety. By controlling the molar ratio of **24/25**/poly- β -cyclodextrin (1:5:20), the ^{19}F -MRI signal was measured and quantified using an external standard (25 mM of NaPF_6). The external standard was used to quantify the amount of **25**, which was used to infer the concentration of **24** because the molar ratios were known. The second mode of imaging, ^1H -MRI, was used to measure the T_1 of the solution, which was affected by the protonation state of **24**. Accordingly, the T_1 of the solution and the concentration of **24** were known, and r_1 could be determined to detect the response. It should be noted that this method does not circumvent the need for knowledge of concentration, but it does provide a way to quantify the concentration of contrast agents to detect responses. A benefit of using ^{19}F as a handle for contrast agent quantification is the minimal background signal of ^{19}F *in vivo*; however, relatively slow ^{19}F relaxation times limit the sensitivity of detection necessitating millimolar levels of contrast agent in tissues.^{72b} A different isotope, ^{18}F , can also be used for dual-mode imaging, but in a much different manner.

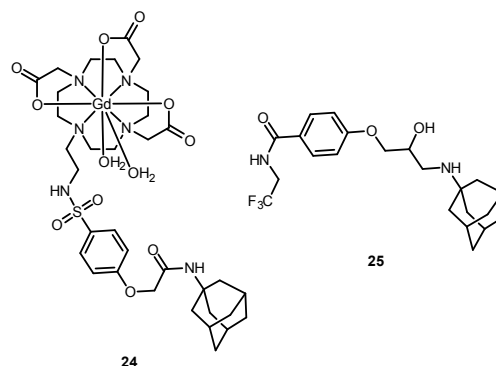


Figure 27. Structure of adamantane-functionalized contrast agents used for ^1H - (**24**) and ^{19}F -MRI (**25**, stereochemistry of hydroxyl group not specified).³⁰

Caravan and co-workers used ^1H -MRI and PET for quantitative pH imaging.²⁷ Their method, in a similar fashion to that used in the previous example, relied on external standards to quantify the concentration of agent present. Instead of using ^{19}F as the handle for concentration determination, they used the positron-emitting isotope ^{18}F . Briefly, PET operates by using a positron-emitting isotope (for example, ^{11}C , ^{13}N , ^{15}O , ^{18}F , ^{64}Cu ,

^{66}Ga , or ^{82}Rb), which can be incorporated into a compound of interest to produce a radiotracer. The radioactive isotope within the radiotracer decays through positron emission, and the emitted positron travels until its energy is low enough to permit interaction with an electron resulting in an annihilation event. The annihilation between a positron and electron produces two gamma rays that travel in opposite ($\sim 180^\circ$) directions. A gamma detector can measure the time difference between two coincident gamma rays to calculate the location of the radiotracer. The gamma ray background of humans is small relative to the proton background, which makes PET extremely sensitive. Additionally, gamma activity can be used to quantify the amount of radiotracer present. Using **26** (Figure 28),²⁷ Caravan and co-workers quantified the amount of contrast agent present using PET imaging with external standards. The second mode of imaging, T_1 -weighted ^1H -MRI, was used to determine the T_1 of the solution. Similar to the previous example, knowing both the T_1 of the solution and the contrast agent concentration allows for r_1 to be determined, and a quantitative response can be measured (Figure 29). An important feature of this dual-mode technique is that the MRI and PET imaging were performed simultaneously (whereas most other dual-mode strategies use sequential imaging), which means that diffusion of the contrast agent would not pose a problem *in vivo*.

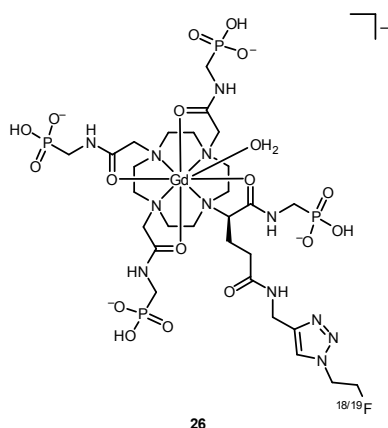


Figure 28. Structure of GdDOTA-4AMP-F (**26**) used for dual-mode PET and ^1H -MRI for quantitative pH measurements.²⁷ Phosphonates are drawn singly protonated because of the expected $\text{p}K_a$ values of the first ($\text{p}K_a \approx 2\text{--}3$) and second ($\text{p}K_a \approx 7\text{--}8$) phosphonate oxygen atoms.

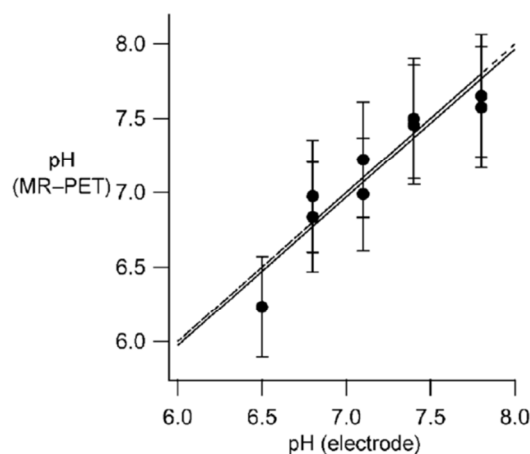


Figure 29. pH determined with the MR/PET technique vs pH determined using a glass electrode. The solid line represents a linear fit of the data and the dashed line represents a hypothetical 1:1 correspondence between the x- and y-axes. Figure adapted with permission from Bimodal MR–PET Agent for Quantitative pH Imaging/L. Frullano, C. Catana, T. Benner, A. D. Sherry and P. Caravan/*Angew. Chem.*, **122**/13. Copyright © 2010 WILEY-VCH Verlag GmbH & Co. KGaA, Weinheim.

In a similar fashion to the example above, Aime and co-workers used ^1H -MRI and SPECT to detect changes in pH using **23a** and its isostructural $^{166}\text{Ho}^{3+}$ -containing analogue as a radiotracer.²⁸ SPECT operates in a similar fashion to PET, but the radioisotope emits gamma rays directly instead of through an indirect annihilation event. The direct emission of gamma rays causes SPECT to have lower sensitivity relative to PET because the radiotracer cannot be detected through coincident gamma rays. A decrease in sensitivity of SPECT means that temporal resolution must suffer to achieve adequate contrast, and longer acquisition periods allow for contrast agents to diffuse to a greater extent. In this example, the radiotracer acted as a calibration standard to infer the concentration of **23a**. Knowing the concentration of **23a** allowed for a pH response to be measured.²⁸ A difference between this MRI-SPECT dual-mode strategy and the previously discussed MRI-PET strategy is that the MRI-SPECT strategy requires sequential imaging, which can allow contrast agent diffusion to occur resulting in increased chances for error. Most of the examples highlighted throughout this review focus on both responding to and quantification of stimuli. It can be argued, however, that quantification of stimuli is not always necessary to obtain important information in a concentration-independent way. To detect a response without quantification, a threshold response must be used.

In the first three examples within the dual-mode section, external standards were used to quantify contrast agents that responded to pH. In this manner, the concentration could be inferred indirectly. Alternatively, dual-mode can be used without any knowledge of the concentration of contrast agent. Recently, Allen and co-workers used CEST and T_1 -weighted ^1H -MRI to demonstrate a response to oxidation using **27** (Figure 30) encapsulated in liposomes.⁴⁸ The use of Eu^{2+} -containing cryptates is potentially advantageous because r_1 increases at ultra-high magnetic field strengths ($\geq 7\text{ T}$),⁸⁸ whereas the r_1 of Gd^{3+} -containing complexes decrease.⁸⁹ Furthermore, higher magnetic field strengths can lead to greater spatial and temporal resolutions that are desirable for diagnostic

scans. However, a limitation with Eu^{2+} is its propensity to oxidize to Eu^{3+} . The oxidation potential of Eu^{2+} can be modulated through structural modifications to the ligand, and some of the reported modifications result in the most positive oxidation potentials (more resistant to oxidation) ever reported in aqueous solution.⁹⁰ Despite the gains in oxidative stability, even the most oxidatively stable of the complexes were oxidized in air. However, Allen and co-workers used the oxidation of Eu^{2+} as an advantageous reaction because of the drastic difference in T_1 -shortening capabilities between Eu^{2+} and Eu^{3+} . Liposome suspensions containing encapsulated **27** were characterized before and after air exposure (oxygen within the air was a convenient source of oxidant), and dynamic light scattering measurements revealed no change in average size or polydispersity of liposomes upon oxidation. It was observed that the T_1 of liposomes containing **27** decreased by up to 86% after oxidation, which is a relatively large decrease in T_1 . Furthermore, the reduction in T_1 after oxidation made the liposomes indistinguishable from water in T_1 -weighted images (Figure 31). In the second imaging mode, CEST, an exchangeable pool of protons was observed 1.2 ppm downfield from bulk water, and the signal was unresponsive to oxidation within the error of the measurements. Accordingly, the CEST signal could be used to monitor the presence of the contrast agent, while the T_1 of the solution containing **27** encapsulated in liposomes reports on response to oxidation (Figure 31). While this method does not quantify the amount of oxidant present, it can report if an oxidation threshold has been crossed. A secondary advantage of using liposomes in this system is to prevent uncomplexed Eu^{3+} from entering the bloodstream. It was observed that the liposomes prevented the release of Eu^{3+} ,⁴⁸ which is a promising implication for *in vivo* studies.

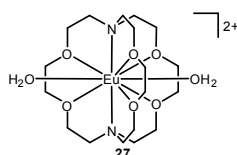


Figure 30. Structure of $\text{Eu}(2.2.2)^{2+}$ (**27**) used for liposome encapsulation to demonstrate a response to oxidation using CEST and T_1 -weighted ^1H -MRI.⁴⁸

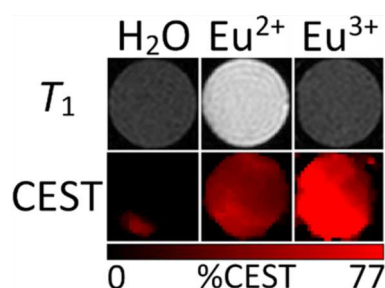


Figure 31. MR phantom images (5 mm tube diameter) at 7 T and 24 °C of water, non-oxidized liposomes containing **27**, and liposomes filled with the Eu^{3+} -containing product of the oxidation of **27**. The top row contains T_1 -weighted images and the bottom row contains CEST maps generated by subtracting presaturation signal intensity at 1.2 ppm from presaturation signal intensity at -1.2 ppm and the difference was divided by the presaturation signal intensity at -1.2 ppm. %CEST represents the decrease in bulk water signal intensity as a result of the presaturation of exchangeable water protons associated with liposomes. Statistical analysis ($n = 6$) suggests that

changes in %CEST are not significant before and after oxidation. Reproduced from Ref. 48 with permission from The Royal Society of Chemistry.

The dual-mode examples so far have been used for *in vitro* imaging, but in the next section we highlight examples that have used internal standards to indirectly measure the concentration of contrast agent, but for *in vivo* imaging.

Dual-Injection

An alternative to using external standards or ratiometric techniques is to use an internal standard to indirectly monitor the biodistribution of a responsive contrast agent. In doing so, one must make the assumption of (or demonstrate) sufficiently similar pharmacokinetics of two separate complexes. Raghunand and co-workers monitored the time-dependent distribution of **28** and **29** (Figure 32) after sequential tail-vein injections.³¹ Previously, Sherry and co-workers had demonstrated the pH-dependency of the r_1 of **28**,¹³ where the hydrogen-bonding network of the pendant arms was influenced by changes in protonation state. Interestingly, **29** is pH-insensitive despite some structural similarities with **28**. Raghunand and co-workers demonstrated that **28** and **29** had comparable biodistribution within the mouse model and that the concentration of **28** could be inferred by tracking **29** through T_1 -weighted images. Using **28** and **29**, *in vivo* pH maps were generated to demonstrate kidney alkalization (Figure 33) induced by treatment with the carbonic anhydrase inhibitor acetazolamide.

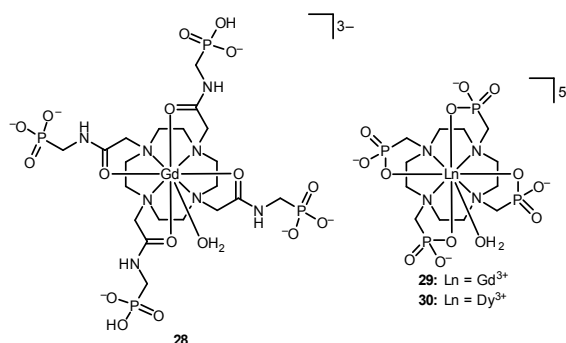


Figure 32. Structure of GdDOTA-4AMP (**28**), GdDOTP (**29**), and DyDOTP (**30**) used to generate *in vivo* pH maps using a dual-injection strategy.^{31,91,92}

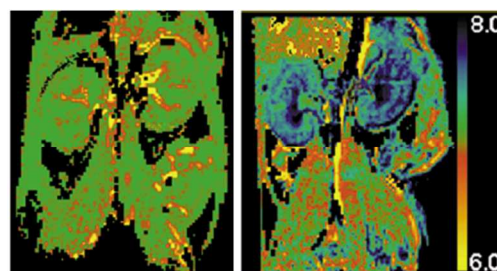


Figure 33. Calculated pH maps of mouse kidneys generated using the dual-injection strategy of a mouse without (left) and with (right) acetazolamide treatment demonstrating alkalization of kidneys. A pH scale bar is on the far right. Figure adapted with permission from Renal and Systemic pH

Imaging by Contrast-Enhanced MRI/N. Raghunand, C. Howison, A. D. Sherry, S. Zhang and R. J. Gillies/*Magn. Reson. Med.*, **49**/2. Copyright © 2003 Wiley-Liss, Inc.

In a subsequent report, Gillies and co-workers applied the dual-injection strategy using **28** and **29** (Figure 32) to generate pH maps of tumors,⁹¹ which they argued is significantly more difficult than imaging kidneys due to the heterogeneous distribution of blood vessels, slower diffusion of agent, and higher protein concentrations of the extracellular fluid. Due to these challenges, the authors accounted for the potential of residual **29** to be present in the tumor microenvironment at the time **28** was injected. To correct for residual **29**, they modeled how quickly **29** washed out of tumors using a bi-exponential equation on a pixel-by-pixel basis and the extrapolated residual signal from **29** was used as a background subtraction for **28** pharmacokinetics. Expectedly, the average pharmacokinetics of **28** and **29** were similar, but the authors observed that local differences (pixel-by-pixel) reduced the apparent pharmacokinetic correlation of the two contrast agents. To correct for these differences, pH maps were calculated using the maximal enhancement per pixel. Using the aforementioned techniques to account for tumor heterogeneity, Gillies and co-workers were able to calculate pH maps of mouse gliomas.⁹¹

In the previous two examples of dual-injection imaging, sequential injections were used. However, the dual-injection strategy does not require sequential injections. A relatively severe limitation of sequential injections is temporal resolution, where images were collected for 1 h after the injection of each contrast agent for the previous two examples. To improve the temporal resolution, two contrast agents can be injected simultaneously.

Recently, a single cocktail approach was developed by Martinez and co-workers using **28** and **30** for pH mapping of tumors.⁹² In the previous approaches, sequential injections were required because **28** and **29** both produce T_1 enhancement such that they would be indistinguishable if injected simultaneously. By using **30** as the pH-insensitive handle to track biodistribution, however, the presence of **30** could be detected by its influence on the rate of phase decoherence of the nuclear dipole moments of neighbouring protons. Importantly, **30** had a negligible influence on T_1 . This approach is a dual-injection, dual-mode strategy because of the use of two contrast agents and detection with both T_1 - and T_2 -weighted imaging. By (1) using a contrast agent cocktail with a controlled molar ratio of **28/30** (1:2) and (2) assuming near identical pharmacokinetics of **28** and **30** based on previous reports comparing **28** and **29**,⁹¹ this strategy was used to produce pH maps of tumors with improved temporal resolution relative to sequential injection strategies (20–90 min vs 120 min).

Throughout this review, pH has been detected in a variety of ways. As previously discussed, pH is an intuitive target for detection because ^1H -MRI directly detects protons and changes in proton-exchange can be used to calculate pH. In the next section, we discuss a rather unique approach to pH detection that involves perturbations in the ligand field of lanthanide ions.

Ligand Field-Induced Chemical Shift

Ln^{3+} ions were once thought to be static spheres of positive charge with unchanging luminescence and magnetic properties due to the limited radial distribution of 4f-orbitals. It has been demonstrated, however, that some Ln^{3+} ions have spectroscopic and magnetic properties that are relatively sensitive to changes

in the coordination environment (ligand field) of the metal ion.^{29,93} Of importance to this review, ligand field changes can influence the effective magnetic moment of Ln^{3+} ions, which is likely due to changes in the geometry of ligand distribution about the metal ion. Recently, Parker and co-workers demonstrated a pH response using ligand field-induced chemical shift.²⁹ Upon moving to acidic pH values, the concentration of **31a** decreased as the protonated form **31b** increased (Figure 34). Specifically, the ^1H resonance frequency (–58 ppm) of a nearby (–6.6 Å) *tert*-butyl group was used to monitor the change in protonation state. As the pH was lowered, the signal intensity at –58 ppm decreased. The response was detected ratiometrically by using an analogous *tert*-butyl group on **32** at –18 ppm. Importantly, **32** did not possess the same pH-dependence as **31a**. Accordingly, the ratio of *tert*-butyl signal intensities (–58 ppm/–18 ppm) in a solution containing **31a/32** (1:1) reported the pH of the solution over a range of 4 to 7 (Figure 35).

It is important to emphasize that this example is not based on a CEST mechanism because an exchangeable proton is not being selectively saturated and, therefore, saturation transfer is not being used. Instead, the ligand field of a Ln^{3+} -containing complex is perturbed through a change in protonation state, and the perturbed ligand field influences the effective magnetic moment. The altered magnetic moment then influences the chemical shift values of nearby protons. While Parker and co-workers did not demonstrate concentration-independence in this example, the response is inherently concentration-independent because of its ratiometric nature, assuming similar kinetic stabilities and that the concentration ratio of the two contrast agents is known and does not change over the course of imaging. A possible avenue for future developments that involve ligand field-induced chemical shifts would be to covalently attach two compounds, such as **31a** and **32**, to ensure that differences in pharmacokinetics are not a concern, but the covalent linkage would need to be long enough to prevent changes in the ligand field of one metal center to influence proton resonances on the other. A separate avenue could be to revisit some of the contrast agents that respond to changes in water coordination number,⁶⁴ because ligand field-induced chemical shift might offer a platform for more ratiometric probes using previously reported chemical responses.

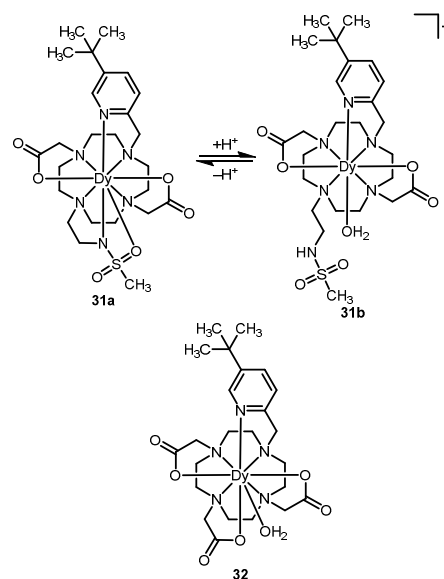


Figure 34. Structure of **31a** and its protonated form **31b** that alter the chemical shift of *tert*-butyl protons through changes in ligand field. The ratiometric pH response was measured using **32** as a secondary compound with a different pH dependence.²⁹

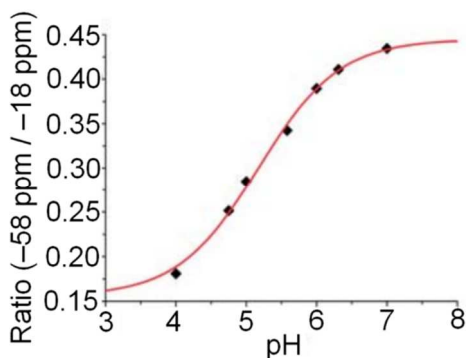


Figure 35. Ratio of *tert*-butyl proton chemical shift intensities of **31a** and **32** as a function of pH. Reproduced from Ref. 29 with permission from The Royal Society of Chemistry.

Conclusions

The challenge of overcoming concentration-dependence in responsive contrast agents for MRI has been approached from many different angles. Ratiometric CEST, ratiometric relaxation rates, dual-mode, dual-injection, and ligand field-induced chemical shift strategies have been employed to push the field towards *in vivo* applicability and, in some cases, have already made the leap to *in vivo* imaging. While there have been substantial developments toward the goal of overcoming concentration-dependence, there is still work to be done. For instance, much of the effort in the area has focused on concentration-independent pH imaging, but the examples of other targets are relatively few. One of the largest limitations of contrast agents that provide contrast through proton exchange is relatively low sensitivity (millimolar concentrations in tissue) because they must provide contrast that is distinguishable from the relatively large proton background *in vivo*. Coupling MRI with the extremely sensitive PET imaging modality still imparts a sensitivity limitation because PET is used to quantify the agent whose response is detected through ¹H imaging techniques. The ligand field-induced chemical shift approach offers an interesting platform for large sensitivity gains because contrast agents can be designed to contain large numbers of chemically equivalent protons to boost the sensitivity. Another limitation with strategies that use a combination of detection methods (multiple CEST frequencies, contrast agents, or pulse sequences) to circumvent concentration-dependence is that the error associated with each detection method is propagated to the final measurement. Additionally, some strategies forgo practical temporal resolutions to obtain exquisite quantification of analyte. Although the results are impressive, the clinical usefulness might not be realized until acquisition times are substantially reduced.

Regardless of the current set of limitations within the field and within the individual strategies, momentum is building toward a new class of contrast agents capable of reporting real time responses *in vivo*. With the advent of the strategies reported in this critical review and, undoubtedly, new strategies to come, one may envision a sharp increase in the number of contrast agents for MRI undergoing clinical trials. Arguably, one of the biggest barriers preventing the clinical application of responsive agents (other than target-specific delivery)⁹⁴ is

concentration-dependence. Accordingly, all progress toward overcoming concentration-dependence in responsive contrast agents for MRI has the potential to significantly and positively impact diagnostic molecular imaging.

Acknowledgements

The authors acknowledge the National Institutes of Health grant EB013663 (M.J.A.) and Wayne State University for a Thomas C. Rumble Graduate Research Fellowship (L.A.E.) and a Schaap Faculty Scholar Award (M.J.A.).

Notes and references

Department of Chemistry, Wayne State University, 5101 Cass Avenue, Detroit, MI 48202, USA. Email: mallen@chem.wayne.edu

- G. Radecki, R. Nargeot, I. O. Jelescu, D. Le Bihan and L. Ciobanu, *Proc. Natl. Acad. Sci. U.S.A.*, 2014, **111**, 8667.
- (a) J. Kowalewski, L. Nordenskiöld, N. Benetis and P.-O. Westlund, *Prog. Nucl. Magn. Reson. Spectrosc.*, 1985, **17**, 141; (b) R. B. Lauffer, *Chem. Rev.*, 1987, **87**, 901; (c) P. Caravan, J. J. Ellison, T. J. McMurry and R. B. Lauffer, *Chem. Rev.*, 1999, **99**, 2293.
- J. Xu, S. J. Franklin, D. W. Whisenhunt, Jr. and K. N. Raymond, *J. Am. Chem. Soc.*, 1995, **117**, 7245.
- E. J. Werner, S. Avedano, M. Botta, B. P. Hay, E. G. Moore, S. Aime and K. N. Raymond, *J. Am. Chem. Soc.*, 2007, **129**, 1870.
- P. Caravan, C. T. Farrar, L. Frullano and R. Uppal, *Contrast Media Mol. Imaging*, 2009, **4**, 89.
- J. Zhang, P. P. Fatouros, C. Shu, J. Reid, L. S. Owens, T. Cai, H. W. Gibson, G. L. Long, F. D. Corwin, Z.-J. Chen and H. C. Dorn, *Bioconjugate Chem.*, 2010, **21**, 610.
- E. Pösel, H. Kloust, U. Tromsdorf, M. Janschel, C. Hahn, C. Maßlo and H. Weller, *ACS Nano*, 2012, **6**, 1619.
- E. M. Gale, N. Kenton and P. Caravan, *Chem. Commun.*, 2013, **49**, 8060.
- J. Martinelli, K. Thangavel, L. Tei and M. Botta, *Chem. Eur. J.*, 2014, **20**, 10944.
- V. S. R. Harrison, C. E. Carney, K. W. Macrenaris and T. J. Meade, *Chem. Commun.*, 2014, **50**, 11469.
- (a) R. A. Moats, S. E. Fraser and T. J. Meade, *Angew. Chem. Int. Ed. Engl.*, 1997, **36**, 726; (b) L. M. Urbanczyk-Pearson, F. J. Femia, J. Smith, G. Parigi, J. A. Duimstra, A. L. Eckermann, C. Luchinat and T. J. Meade, *Inorg. Chem.*, 2008, **47**, 56.
- (a) W.-h. Li, S. E. Fraser and T. J. Meade, *J. Am. Chem. Soc.*, 1999, **121**, 1413; (b) W.-h. Li, G. Parigi, M. Fragai, C. Luchinat and T. J. Meade, *Inorg. Chem.*, 2002, **41**, 4018.
- S. Zhang, K. Wu and A. D. Sherry, *Angew. Chem. Int. Ed.*, 1999, **38**, 3192.
- S. Aime, M. Botta, S. G. Crich, G. Giovenzana, G. Palmisano and M. Sisti, *Chem. Commun.*, 1999, 1577.
- R. Hovland, C. Gløgård, A. J. Aasen and J. Klaveness, *J. Chem. Soc., Perkin Trans. 2*, 2001, 929.
- M. Woods, G. E. Kiefer, S. Bott, A. Castillo-Muzquiz, C. Eshelbrenner, L. Michaudet, K. McMillan, S. D. K. Mudigunda, D. Ogrin, G. Tircsó, S. Zhang, P. Zhao and A. D. Sherry, *J. Am. Chem. Soc.*, 2004, **126**, 9248.

- 17 É. Tóth, R. D. Bolskar, A. Borel, G. González, L. Helm, A. E. Merbach, B. Sitharaman and L. J. Wilson, *J. Am. Chem. Soc.*, 2005, **127**, 799.
- 18 M. M. Ali, M. Woods, P. Caravan, A. C. L. Opina, M. Spiller, J. C. Fettinger and A. D. Sherry, *Chem. Eur. J.*, 2008, **14**, 7250.
- 19 S. Zhang, K. Zhou, G. Huang, M. Takahashi, A. D. Sherry and J. Gao, *Chem. Commun.*, 2013, **49**, 6418.
- 20 Z. Baranyai, G. A. Rolla, R. Negri, A. Forgács, G. B. Giovenzana and L. Tei, *Chem. Eur. J.*, 2014, **20**, 2933.
- 21 S. Aime, A. Barge, D. D. Castelli, F. Fedeli, A. Mortillaro, F. U. Nielsen and E. Terreno, *Magn. Reson. Med.*, 2002, **47**, 639.
- 22 (a) S. Aime, D. D. Castelli and E. Terreno, *Angew. Chem.*, 2002, **114**, 4510; (b) E. Terreno, D. D. Castelli, G. Cravotto, L. Milone and S. Aime, *Invest. Radiol.*, 2004, **39**, 235.
- 23 G. Liu, Y. Li, V. R. Sheth and M. D. Pagel, *Molecular Imaging*, 2012, **11**, 47.
- 24 S. J. Dorazio, A. O. Olatunde, J. A. Spornyak and J. R. Morrow, *Chem. Commun.*, 2013, **49**, 10025.
- 25 S. Aime, F. Fedeli, A. Sanino and E. Terreno, *J. Am. Chem. Soc.*, 2006, **128**, 11326.
- 26 E. Gianolio, S. Porto, R. Napolitano, S. Baroni, G. B. Giovenzana and S. Aime, *Inorg. Chem.*, 2012, **51**, 7210.
- 27 L. Frullano, C. Catana, T. Benner, A. D. Sherry and P. Caravan, *Angew. Chem.*, 2010, **122**, 2432.
- 28 E. Gianolio, L. Maciocco, D. Imperio, G. B. Giovenzana, F. Simonelli, K. Abbas, G. Bisi and S. Aime, *Chem. Commun.*, 2011, **47**, 1539.
- 29 P. Harvey, A. M. Blamire, J. I. Wilson, K.-L. N. A. Finney, A. M. Funk, P. K. Senanayake and D. Parker, *Chem. Sci.*, 2013, **4**, 4251.
- 30 E. Gianolio, R. Napolitano, F. Fedeli, F. Arena and S. Aime, *Chem. Commun.*, 2009, 6044.
- 31 N. Raghunand, C. Howison, A. D. Sherry, S. Zhang and R. J. Gillies, *Magn. Reson. Med.*, 2003, **49**, 249.
- 32 N. McVicar, A. X. Li, M. Suchý, R. H. E. Hudson, R. S. Menon and R. Bartha, *Magn. Reson. Med.*, 2013, **70**, 1016.
- 33 D. D. Castelli, E. Terreno and S. Aime, *Angew. Chem. Int. Ed.*, 2011, **50**, 1798.
- 34 S. Zhang, C. R. Malloy and A. D. Sherry, *J. Am. Chem. Soc.*, 2005, **127**, 17572.
- 35 N. McDannold, S. L. Fossheim, H. Rasmussen, H. Martin, N. Vykhodtseva and K. Hynynen, *Radiology*, 2004, **230**, 743.
- 36 S. Langereis, J. Keupp, J. L. J. van Velthoven, I. H. C. de Roos, D. Burdinski, J. A. Pikkemaat and H. Grüll, *J. Am. Chem. Soc.*, 2009, **131**, 1380.
- 37 I.-R. Jeon, J. G. Park, C. R. Haney and T. D. Harris, *Chem. Sci.*, 2014, **5**, 2461.
- 38 R. Trokowski, J. Ren, F. K. Kálmán and A. D. Sherry, *Angew. Chem. Int. Ed.*, 2005, **44**, 6920.
- 39 E. L. Que, E. Gianolio, S. L. Baker, A. P. Wong, S. Aime and C. J. Chang, *J. Am. Chem. Soc.*, 2009, **131**, 8527.
- 40 E. A. Weitz, C. Lewandowski, E. D. Smolensky, M. Marjańska and V. C. Pierre, *ACS Nano*, 2013, **7**, 5842.
- 41 S. Aime, M. Botta, E. Gianolio and E. Terreno, *Angew. Chem. Int. Ed.*, 2000, **39**, 747.
- 42 C. Tu, E. A. Osborne and A. Y. Louie, *Tetrahedron*, 2009, **65**, 1241.
- 43 S. J. Ratnakar, T. C. Soesbe, L. L. Lumata, Q. N. Do, S. Viswanathan, C.-Y. Lin, A. D. Sherry and Z. Kovacs, *J. Am. Chem. Soc.*, 2013, **135**, 14904.
- 44 P. B. Tsitovich, J. A. Spornyak and J. R. Morrow, *Angew. Chem.*, 2013, **125**, 14247.
- 45 B. Song, Y. Wu, M. Yu, P. Zhao, C. Zhou, G. E. Kiefer and A. D. Sherry, *Dalton Trans.*, 2013, **42**, 8066.
- 46 G. S. Loving, S. Mukherjee and P. Caravan, *J. Am. Chem. Soc.*, 2013, **135**, 4620.
- 47 G. Liu, Y. Li and M. D. Pagel, *Magn. Reson. Med.*, 2007, **58**, 1249.
- 48 L. A. Ekanger, M. M. Ali and M. J. Allen, *Chem. Commun.*, 2014, **50**, 14835.
- 49 M. P. Lowe, *Curr. Pharm. Biotechnol.*, 2004, **5**, 519.
- 50 J. Zhou and P. C. M. van Zijl, *Prog. Nucl. Magn. Reson. Spectrosc.*, 2006, **48**, 109.
- 51 B. Yoo and M. D. Pagel, *Front. Biosci.*, 2008, **13**, 1733.
- 52 F. Hyodo, B. P. Soule, K.-i. Matsumoto, S. Matusmoto, J. A. Cook, E. Hyodo, A. L. Sowers, M. C. Krishna and J. B. Mitchell, *J. Pharm. Pharmacol.*, 2008, **60**, 1049.
- 53 E. Pérez-Mayoral, V. Negri, J. Soler-Padrós, S. Cerdán and P. Ballesteros, *Eur. J. Radiol.*, 2008, **67**, 453.
- 54 S. Aime, D. D. Castelli, S. G. Crich, E. Gianolio and E. Terreno, *Acc. Chem. Res.*, 2009, **42**, 822.
- 55 M. M. Ali, G. Liu, T. Shah, C. A. Flask and M. D. Pagel, *Acc. Chem. Res.*, 2009, **42**, 915.
- 56 L. M. De Leon-Rodriguez, A. J. M. Lubag, C. R. Malloy, G. V. Martinez, R. J. Gillies and A. D. Sherry, *Acc. Chem. Res.*, 2009, **42**, 948.
- 57 E. L. Que and C. J. Chang, *Chem. Soc. Rev.*, 2010, **39**, 51.
- 58 K. Hanaoka, *Chem. Pharm. Bull.*, 2010, **58**, 1283.
- 59 G. Angelovski and I. Mamedov, *Curr. Inorg. Chem.*, 2011, **1**, 76.
- 60 C. Tu, E. A. Osborne and A. Y. Louie, *Ann. Biomed. Eng.*, 2011, **39**, 1335.
- 61 G.-L. Davies, I. Kramberger and J. J. Davis, *Chem. Commun.*, 2013, **49**, 9704.
- 62 C. Shen and E. J. New, *Curr. Opin. Chem. Biol.*, 2013, **17**, 158.
- 63 A. D. Sherry and Y. Wu, *Curr. Opin. Chem. Biol.*, 2013, **17**, 167.
- 64 C. Tu and A. Y. Louie, *NMR Biomed.*, 2013, **26**, 781.
- 65 T. C. Soesbe, Y. Wu and A. D. Sherry, *NMR Biomed.*, 2013, **26**, 829.
- 66 M. C. Heffern, L. M. Matosziuk and T. J. Meade, *Chem. Rev.*, 2014, **114**, 4496.
- 67 P. B. Tsitovich, P. J. Burns, A. M. McKay and J. R. Morrow, *J. Inorg. Biochem.*, 2014, **133**, 143.
- 68 Q. N. Do, J. S. Ratnakar, Z. Kovács and A. D. Sherry, *ChemMedChem*, 2014, **9**, 1116.
- 69 (a) K. M. Ward and R. S. Balaban, *Magn. Reson. Med.*, 2000, **44**, 799; (b) S. Forsén and R. A. Hoffman, *J. Chem. Phys.*, 1963, **39**, 2892.
- 70 M. Zaiss and P. Bachert, *Phys. Med. Biol.*, 2013, **58**, R221.
- 71 G. Liu, M. Moake, Y.-e. Har-el, C. M. Long, K. W. Y. Chan, A. Cardona, M. Jamil, P. Walczak, A. A. Gilad, G. Sgouros, P. C. M. van Zijl, J. W. M. Bulte and M. T. McMahon, *Magn. Reson. Med.*, 2012, **67**, 1106.
- 72 (a) B. Bleaney, *J. Magn. Reson.*, 1972, **8**, 91; (b) K. H. Chalmers, A. M. Kenwright, D. Parker and A. M. Blamire, *Magn. Reson. Med.*, 2011, **66**, 931.

Metallomics

- 1 73 P. W. Selwood, *J. Am. Chem. Soc.*, 1933, **55**, 4869.
- 2 74 (a) J. Hammell, L. Buttarazzi, C.-H. Huang and J. R. Morrow, *Inorg.*
- 3 *Chem.*, 2011, **50**, 4857; (b) Z. Lin and M. J. Allen, *Dyes Pigments*,
- 4 2014, **110**, 261; (c) J.-C. G. Bünzli and S. V. Eliseeva, *Chem. Sci.*,
- 5 2013, **4**, 1939.
- 6 75 S. Zhang, P. Winter, K. Wu and A. D. Sherry, *J. Am. Chem. Soc.*,
- 7 2001, **123**, 1517.
- 8 76 S. Aime, A. Barge, M. Botta, A. S. De Sousa and D. Parker, *Angew.*
- 9 *Chem. Int. Ed.*, 1998, **37**, 2673.
- 10 77 D. L. Longo, P. Z. Sun, L. Consolino, F. C. Michelotti, F. Uggeri and
- 11 S. Aime, *J. Am. Chem. Soc.*, 2014, **136**, 14333.
- 12 78 S. Aime, M. Botta, M. Fasano and E. Terreno, *Acc. Chem. Res.*,
- 13 1999, **32**, 941.
- 14 79 V. Catanzaro, C. V. Gringeri, V. Menchise, S. Padovan, C. Boffa, W.
- 15 Dastrù, L. Chaabane, G. Digilio and S. Aime, *Angew. Chem. Int. Ed.*,
- 16 2013, **52**, 3926.
- 17 80 M. Botta and L. Tei, *Eur. J. Inorg. Chem.*, 2012, **2012**, 1945.
- 18 81 J. K. Alford, A. G. Sorensen, T. Benner, B. A. Chronik, W. B.
- 19 Handler, T. J. Scholl, G. Madan and P. Caravan, *Proc. Intl. Soc.*
- 20 *Magn. Reson. Med.*, 2011, **19**, 452.
- 21 82 E. D. Smolensky, M. Marjańska and V. C. Pierre, *Dalton Trans.*,
- 22 2012, **41**, 8039.
- 23 83 J. M. Perez, L. Josephson, T. O'Loughlin, D. Högemann and R.
- 24 Weissleder, *Nat. Biotech.*, 2002, **20**, 816.
- 25 84 M. Zhao, L. Josephson, Y. Tang and R. Weissleder, *Angew. Chem.*
- 26 *Int. Ed.*, 2003, **42**, 1375.
- 27 85 M. V. Yigit, D. Mazumdar and Y. Lu, *Bioconjugate Chem.*, 2008, **19**,
- 28 412.
- 29 86 J. M. Perez, F. J. Simeone, Y. Saeki, L. Josephson and R. Weissleder,
- 30 *J. Am. Chem. Soc.*, 2003, **125**, 10192.
- 31 87 V. Rüdiger, A. Eliseev, S. Simova, H.-J. Schneider, M. J. Blandamer,
- 32 P. M. Cullis and A. J. Meyer, *J. Chem. Soc., Perkin Trans. 2*, 1996,
- 33 2119.
- 34 88 (a) J. Garcia, J. Neelavalli, E. M. Haacke and M. J. Allen, *Chem.*
- 35 *Commun.*, 2011, **47**, 12858; (b) J. Garcia, A. N. W. Kuda-
- 36 Wedagedara and M. J. Allen, *Eur. J. Inorg. Chem.*, 2012, **2012**, 2135;
- 37 (c) J. Garcia and M. J. Allen, *Inorg. Chim. Acta*, 2012, **393**, 324.
- 38 89 A. N. W. Kuda-Wedagedara and M. J. Allen, *Analyst*, 2014, **139**,
- 39 4401.
- 40 90 (a) N.-D. H. Gamage, Y. Mei, J. Garcia and M. J. Allen, *Angew.*
- 41 *Chem. Int. Ed.*, 2010, **49**, 8923; (b) L. Burai, É. Tóth, S. Seibig, R.
- 42 Scopelliti and A. E. Merbach, *Chem. Eur. J.*, 2000, **6**, 3761; (c) E. L.
- 43 Yee, O. A. Gansow and M. J. Weaver, *J. Am. Chem. Soc.*, 1980, **102**,
- 44 2278.
- 45 91 M. L. Garcia-Martin, G. V. Martinez, N. Raghunand, A. D. Sherry, S.
- 46 Zhang and R. J. Gillies, *Magn. Reson. Med.*, 2006, **55**, 309.
- 47 92 G. V. Martinez, X. Zhang, M. L. Garcia-Martín, D. L. Morse, M.
- 48 Woods, A. D. Sherry and R. J. Gillies, *NMR Biomed.*, 2011, **24**,
- 49 1380.
- 50 93 D. J. Averill and M. J. Allen, *Inorg. Chem.*, 2014, **53**, 6257.
- 51 94 (a) P. Caravan, *Chem. Soc. Rev.*, 2006, **35**, 512; (b) S. M.
- 52 Vithanarachchi and M. J. Allen, *Current Molecular Imaging*, 2012, **1**,
- 53 12.
- 54
- 55
- 56
- 57
- 58
- 59
- 60